# Supplementary Material for "Quantifying Magnetic Moments with Phase-Based Electron-Optical Nanomagnetometry"


Hangbo Su[a], Xianhui Ye[a], Jiaqi Su[a], Yuying Liu[a], Zian Li[a,*], András Kovács[b], Rafal E. Dunin-Borkowski[b], Marco Beleggia[c]

[a] *School of Physical Science and Technology, Guangxi University, Nanning, 530004, Guangxi, China*
[b] *Ernst Ruska-Centre for Microscopy and Spectroscopy with Electrons, Forschungszentrum Jülich GmbH, Jülich, 52425, Germany*
[c] *Department of Physics, University of Modena and Reggio Emilia, Modena, 41125, Italy*

---

*Corresponding author.
*Email address:* `zianli@gxu.edu.cn` (Zian Li)

**Supplementary Materials**

*0.1. Supplementary Note 1: Detailed Derivation of the Relation Between Inductive Moment and True magnetic Moment*

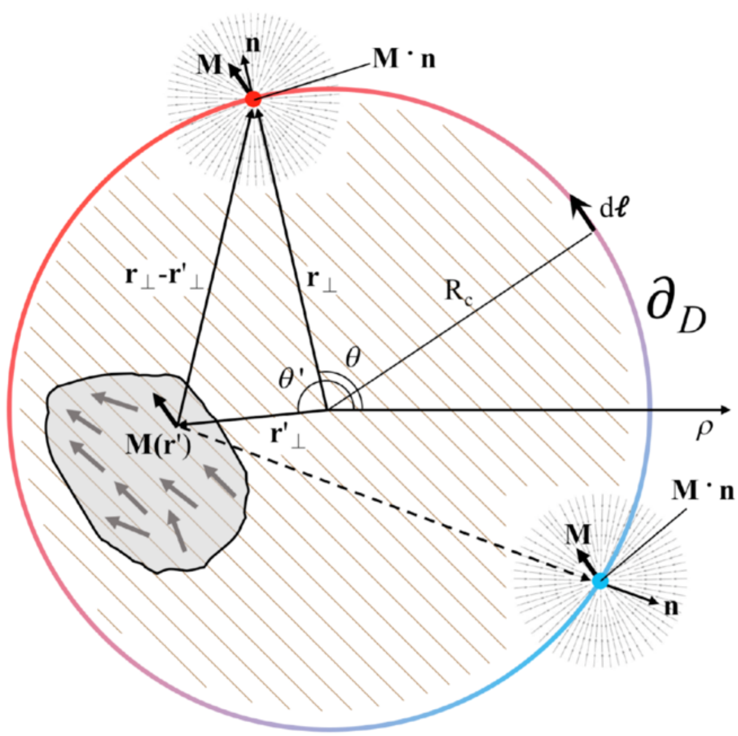


Figure S1: Effect of demagnetizing fields: for circular paths (left), the demagnetizing field **m**H is uniform, leading to a direct relationship (Eq.7 in main text); for noncircular shapes (right), $\mathbf{m}_\mathrm{H}$ becomes integration path dependent.

**Alt text:** A schematic comparison of circular and noncircular integration paths around a magnetized object. The circular path illustrates a uniform demagnetizing-field contribution, whereas the noncircular path illustrates a path-dependent contribution.

This note provides a comprehensive derivation of the relationship between the inductive moment $\mathbf{m}^\mathrm{B}$ and the true magnetic moment $\mathbf{m}$, expanding upon the main text. We begin with the expression for the inductive moment obtained via phase integration and derive the general form that includes the demagnetizing-field contribution.

Starting from Eq.7 in the main text, the inductive moment is expressed as

$$\mathbf{m}^{\mathrm{B}} = \frac{1}{\mu_0} \int_{-\infty}^{+\infty} \mathrm{d}z \oint_{\partial D} A_z(\mathbf{r})\,\mathrm{d}\ell, \tag{1}$$

where $\partial D$ is a closed-path in the plane perpendicular to the electron beam, and $\mathrm{d}\ell$ is the tangent line element. The magnetic vector potential $\mathbf{A}$ is given by the dipole expression

$$\mathbf{A}(\mathbf{r}) = \frac{\mu_0}{4\pi} \iiint_{\mathbb{R}^3} \mathbf{M}(\mathbf{r}') \times \frac{\mathbf{r}-\mathbf{r}'}{|\mathbf{r}-\mathbf{r}'|^3} \mathrm{d}^3\mathbf{r}'. \tag{2}$$

Substituting this into the expression for $\mathbf{m}^{\mathrm{B}}$ yields

$$\mathbf{m}^{\mathrm{B}} = \frac{1}{4\pi} \iiint_{\mathbb{R}^3} \mathrm{d}^3\mathbf{r}' \int_{-\infty}^{+\infty} \mathrm{d}z \oint_{\partial D} \mathrm{d}\ell \left[\mathbf{M}(\mathbf{r}') \times \frac{\mathbf{r}-\mathbf{r}'}{|\mathbf{r}-\mathbf{r}'|^3}\right]_z. \tag{3}$$

Only the $z$-component of the cross product contributes. Using $\mathbf{r} = (\mathbf{r}_\perp, z)$ and $\mathbf{r}' = (\mathbf{r}'_\perp, z')$, we write

$$\left[\mathbf{M}(\mathbf{r}') \times \frac{\mathbf{r}-\mathbf{r}'}{|\mathbf{r}-\mathbf{r}'|^3}\right]_z = \left[\mathbf{M}_\perp(\mathbf{r}') \times \frac{\mathbf{r}_\perp-\mathbf{r}'_\perp}{|\mathbf{r}_\perp-\mathbf{r}'_\perp|^2 + (z-z')^2)^{3/2}}\right]_z, \tag{4}$$

where $\mathbf{M}_\perp = (M_x, M_y)$. The $z$-integration can be performed using the standard result

$$\int_{-\infty}^{+\infty} \frac{\mathrm{d}z}{[|\mathbf{r}_\perp-\mathbf{r}'_\perp|^2 + (z-z')^2]^{3/2}} = \frac{2}{|\mathbf{r}_\perp-\mathbf{r}'_\perp|^2}. \tag{5}$$

This simplifies the expression to

$$\mathbf{m}^{\mathrm{B}} = \frac{1}{2\pi} \iiint_{\mathbb{R}^3} \mathrm{d}^3\mathbf{r}' \oint_{\partial D} \mathrm{d}\ell \left[\mathbf{M}_\perp(\mathbf{r}') \times \frac{\mathbf{r}_\perp-\mathbf{r}'_\perp}{|\mathbf{r}_\perp-\mathbf{r}'_\perp|^2}\right]_z. \tag{6}$$

Writing the cross product explicitly gives

$$\mathbf{m}^{\mathrm{B}} = \frac{1}{2\pi} \iiint_{\mathbb{R}^3} \mathrm{d}^3\mathbf{r}' \oint_{\partial D} \mathrm{d}\ell\, \hat{\mathbf{n}} \times \left[\mathbf{M}(\mathbf{r}') \times \frac{\mathbf{r}_\perp - \mathbf{r}'_\perp}{|\mathbf{r}_\perp - \mathbf{r}'_\perp|^2}\right], \tag{7}$$

where $\hat{\mathbf{n}}$ is the unit normal to the integration path, and we have reinstated the full magnetization vector $\mathbf{M}$ noting that the $z$-component does not contribute to the in-plane cross product.

Applying the vector identity $\mathbf{a} \times (\mathbf{b} \times \mathbf{c}) = \mathbf{b}(\mathbf{a} \cdot \mathbf{c}) - \mathbf{c}(\mathbf{a} \cdot \mathbf{b})$ yields

$$\begin{aligned}\mathbf{m}^{\mathrm{B}} = &\frac{1}{2\pi} \iiint_{\mathbb{R}^3} \mathbf{M}(\mathbf{r}')\mathrm{d}^3\mathbf{r}' \oint_{\partial D} \mathrm{d}\ell\, \hat{\mathbf{n}} \cdot \frac{\mathbf{r}_\perp - \mathbf{r}'_\perp}{|\mathbf{r}_\perp - \mathbf{r}'_\perp|^2} \\ &- \frac{1}{2\pi} \iiint_{\mathbb{R}^3} \mathrm{d}^3\mathbf{r}' \oint_{\partial D} \mathrm{d}\ell\, \left[\hat{\mathbf{n}} \cdot \mathbf{M}(\mathbf{r}')\right] \frac{\mathbf{r}_\perp - \mathbf{r}'_\perp}{|\mathbf{r}_\perp - \mathbf{r}'_\perp|^2}.\end{aligned} \tag{8}$$

The first term contains the closed-path integral

$$I_1 = \frac{1}{2\pi} \oint_{\partial D} \mathrm{d}\ell\, \hat{\mathbf{n}} \cdot \frac{\mathbf{r}_\perp - \mathbf{r}'_\perp}{|\mathbf{r}_\perp - \mathbf{r}'_\perp|^2}. \tag{9}$$

Noting that

$$\frac{\mathbf{r}_\perp - \mathbf{r}'_\perp}{|\mathbf{r}_\perp - \mathbf{r}'_\perp|^2} = \nabla \log |\mathbf{r}_\perp - \mathbf{r}'_\perp|, \tag{10}$$

we apply Green's theorem to convert the path integral to an area integral:

$$\begin{aligned}I_1 &= \frac{1}{2\pi} \oint_{\partial D} \mathrm{d}\ell\, \hat{\mathbf{n}} \cdot \nabla \log |\mathbf{r}_\perp - \mathbf{r}'_\perp| \\ &= \frac{1}{2\pi} \iint_D \mathrm{d}^2\mathbf{r}_\perp\, \nabla^2 \log |\mathbf{r}_\perp - \mathbf{r}'_\perp|.\end{aligned} \tag{11}$$

Using the identity $\nabla^2 \log |\mathbf{r}_\perp - \mathbf{r}'_\perp| = 2\pi\delta^2(\mathbf{r}_\perp - \mathbf{r}'_\perp)$, we obtain

$$I_1 = \iint_D \mathrm{d}^2\mathbf{r}_\perp\, \delta^2(\mathbf{r}_\perp - \mathbf{r}'_\perp) = \begin{cases} 1, & \mathbf{r}'_\perp \in D, \\ 0, & \mathbf{r}'_\perp \notin D. \end{cases} \tag{12}$$

Thus the first term in Eq. (8) evaluates to $\mathbf{m}$ when the integration over $\mathbf{r}'_\perp$ is restricted to the region inside $D$. Since the magnetization $\mathbf{M}(\mathbf{r}')$ vanishes outside the sample, and the sample is fully enclosed by $D$, this term exactly equals the true magnetic moment $\mathbf{m}$.

The second term in Eq. (8) is path-dependent. Defining

$$\mathbf{m}_{\mathrm{H}}(D, \mathbf{M}) = \frac{1}{2\pi} \iiint_{\mathbb{R}^3} \mathrm{d}^3\mathbf{r}' \oint_{\partial D} \mathrm{d}\ell \; [\hat{\mathbf{n}} \cdot \mathbf{M}(\mathbf{r}')] \, \frac{\mathbf{r}_\perp - \mathbf{r}'_\perp}{|\mathbf{r}_\perp - \mathbf{r}'_\perp|^2}, \tag{13}$$

we obtain the general relation

$$\mathbf{m}^{\mathrm{B}} = \mathbf{m} - \mathbf{m}_{\mathrm{H}}(D, \mathbf{M}). \tag{14}$$

This term can be interpreted as the effective contribution from demagnetizing fields arising because the integration domain $D \otimes \mathbb{R}$ is magnetized by the sample's dipoles.

For a circular path of radius $R$ centered at the origin, the integral can be evaluated explicitly. Using cylindrical coordinates and the fact that for a uniformly magnetized sample the demagnetizing field inside an infinite circular cylinder is uniform, one obtains

$$\mathbf{m}_{\mathrm{H}} = \left[\frac{1}{2}m_x, \frac{1}{2}m_y, 0\right]. \tag{15}$$

Hence

$$\mathbf{m}^{\mathrm{B}} = \left[\frac{1}{2}m_x, \frac{1}{2}m_y, m_z\right]. \tag{16}$$

This result reproduces Eq. (22) of Beleggia et al. [1]. For elliptical paths, the in-plane components are reduced by the corresponding planar demagnetization factors $N_{x,y}$ of an infinite elliptical cylinder [2].

*Supplementary Note 2: Volume Integral of the B-field for Uniform Magnetization*

An equivalent derivation can be performed by integrating the magnetic induction $\mathbf{B}$ directly over the cylinder $D \otimes \mathbb{R}$ and relating it to the magnetization through the magnetostatic field equations. For a uniformly magnetized ellipsoid, the demagnetizing field is $\mathbf{H}_d = -N_i \mathbf{M}$ along each principal axis, leading to the same relationship between $\mathbf{m}^{\mathrm{B}}$ and $\mathbf{m}$. This approach is particularly useful for interpreting the volume-averaged demagnetization factors used in experimental analyses.

For a magnetized body with magnetization $\mathbf{M}(\mathbf{r})$, the magnetic vector potential $\mathbf{A}(\mathbf{r})$ can be expressed as [3]

$$\mathbf{A}(\mathbf{r}) = \frac{\mu_0}{4\pi} \iiint_{\mathbb{R}^3} \frac{\nabla' \times \mathbf{M}(\mathbf{r}')}{|\mathbf{r} - \mathbf{r}'|} \, \mathrm{d}^3 r' + \frac{\mu_0}{4\pi} \oint_S \frac{\mathbf{M}(\mathbf{r}') \times \mathbf{n}'}{|\mathbf{r} - \mathbf{r}'|} \, \mathrm{d}a'. \tag{17}$$

In the main text it was shown that the volume integrals of $\mathbf{B}$ coincide for non-uniform and uniform magnetization. We may therefore restrict the discussion to uniform magnetization $\mathbf{M} = \text{const}$ without loss of generality.

Define the magnetic-moment–like quantity constructed from the induction field as

$$\mathbf{m}^{\mathrm{B}} \equiv \frac{1}{\mu_0} \iiint_{\mathbb{R}^3} \mathbf{B} \, \mathrm{d}^3 r, \tag{18}$$

where $\mathbf{B} = \boldsymbol{\nabla} \times \mathbf{A}$. Inserting the surface-term of $\mathbf{A}$ (the volume term vanishes for uniform $\mathbf{M}$) gives

$$\mathbf{m}^{\mathrm{B}} = \frac{1}{4\pi} \iiint_{\mathbb{R}^3} \boldsymbol{\nabla} \times \left( \oint_S \frac{\mathbf{M} \times \mathbf{n}'}{|\mathbf{r} - \mathbf{r}'|} \, \mathrm{d}a' \right) \mathrm{d}^3 r. \tag{19}$$

Applying the vector identity

$$\boldsymbol{\nabla}(\mathbf{a} \times \mathbf{b}) = \mathbf{a}(\boldsymbol{\nabla} \cdot \mathbf{b}) - \mathbf{b}(\boldsymbol{\nabla} \cdot \mathbf{a}) + (\mathbf{b} \cdot \boldsymbol{\nabla})\mathbf{a} - (\mathbf{a} \cdot \boldsymbol{\nabla})\mathbf{b},$$

with $\mathbf{a} = \mathbf{M}$ (constant) and $\mathbf{b} = \mathbf{n}'/|\mathbf{r} - \mathbf{r}'|$, we obtain

$$\begin{aligned}
\mathbf{m}^{\mathrm{B}} = \frac{1}{4\pi} \iiint_{\mathbb{R}^3} \mathbf{M} \, \mathrm{d}^3 r \, &\left( \boldsymbol{\nabla} \cdot \oint_{S'} \frac{\mathbf{n}'}{|\mathbf{r} - \mathbf{r}'|} \, \mathrm{d}a' \right) \\
&- \frac{1}{4\pi} \iiint_{\mathbb{R}^3} \mathrm{d}^3 r \oint_{S'} \frac{\mathbf{n}'}{|\mathbf{r} - \mathbf{r}'|} (\boldsymbol{\nabla} \cdot \mathbf{M}) \, \mathrm{d}a' \\
&+ \frac{1}{4\pi} \iiint_{\mathbb{R}^3} \mathrm{d}^3 r \oint_{S'} \left( \frac{\mathbf{n}'}{|\mathbf{r} - \mathbf{r}'|} \cdot \boldsymbol{\nabla} \right) \mathbf{M} \, \mathrm{d}a' \\
&- \frac{1}{4\pi} \iiint_{\mathbb{R}^3} \mathrm{d}^3 r \, (\mathbf{M} \cdot \boldsymbol{\nabla}) \oint_{S'} \frac{\mathbf{n}'}{|\mathbf{r} - \mathbf{r}'|} \, \mathrm{d}a'. \qquad (20)
\end{aligned}$$

We now analyze the four terms separately.

**First term.** Since $\int_{\mathbb{R}^3} \mathbf{M} \, \mathrm{d}^3 r = \mathbf{m}$, the first term reduces to $\mathbf{m}$ multiplied by

$$\begin{aligned}
\frac{1}{4\pi} \boldsymbol{\nabla} \cdot \oint_{S'} \frac{\mathbf{n}'}{|\mathbf{r} - \mathbf{r}'|} \, \mathrm{d}a' &= \frac{1}{4\pi} \oint_{S'} \boldsymbol{\nabla} \cdot \left( \frac{\mathbf{n}'}{|\mathbf{r} - \mathbf{r}'|} \right) \mathrm{d}a' && (21) \\
&= \frac{1}{4\pi} \oint_{S'} \mathbf{n}' \cdot \boldsymbol{\nabla} \left( \frac{1}{|\mathbf{r} - \mathbf{r}'|} \right) \mathrm{d}a' && (22) \\
&= -\frac{1}{4\pi} \oint_{S'} \mathbf{n}' \cdot \boldsymbol{\nabla}' \left( \frac{1}{|\mathbf{r} - \mathbf{r}'|} \right) \mathrm{d}a' && (23) \\
&= -\frac{1}{4\pi} \oint_{S'} \mathrm{d}\mathbf{a}' \cdot \boldsymbol{\nabla}' \left( \frac{1}{|\mathbf{r} - \mathbf{r}'|} \right) && (24) \\
&= \frac{1}{4\pi} \oint_{S'} \mathrm{d}\Omega = 1. && (25)
\end{aligned}$$

Here we used the definition of the solid-angle element

$$\mathrm{d}\Omega = -\, \mathrm{d}\mathbf{a}' \cdot \boldsymbol{\nabla}' \left( \frac{1}{|\mathbf{r} - \mathbf{r}'|} \right),$$

and the fact that the solid angle subtended by a closed surface enclosing the field point equals $4\pi$. Hence the first term contributes precisely $\mathbf{m}$.

**Second and third terms.** Because $\mathbf{M}$ is constant, $\boldsymbol{\nabla} \cdot \mathbf{M} = 0$ and $\boldsymbol{\nabla}\mathbf{M} = 0$; consequently both terms vanish.

**Fourth term.** This term corresponds to the volume integral of the demagnetizing field. Defining the demagnetizing tensor

$$\mathbf{N}(\mathbf{r}) = \frac{1}{4\pi}\nabla \oint_{S'} \frac{\mathbf{n}'}{|\mathbf{r}-\mathbf{r}'|}\,\mathrm{d}a', \tag{26}$$

the fourth term can be written as

$$-\frac{1}{4\pi}\iiint_{\mathbb{R}^3} (\mathbf{M}\cdot\boldsymbol{\nabla}) \oint_{S'} \frac{\mathbf{n}'}{|\mathbf{r}-\mathbf{r}'|}\,\mathrm{d}a'\,\mathrm{d}^3r = -\iiint_{\mathbb{R}^3} \mathbf{N}(\mathbf{r})\cdot\mathbf{M}\,\mathrm{d}^3r.$$

For uniform magnetization, $\mathbf{N}(\mathbf{r})\cdot\mathbf{M}$ is the demagnetizing field $\mathbf{H}_d(\mathbf{r})$.

Thus,

$$\mathbf{m}^{\mathrm{B}} = \mathbf{m} - \iiint_{\mathbb{R}^3} \mathbf{N}(\mathbf{r})\cdot\mathbf{M}\,\mathrm{d}^3r. \tag{27}$$

Introducing the volume-averaged demagnetizing tensor

$$\bar{\mathbf{N}} = \frac{1}{V}\iiint_{\mathbb{R}^3} \mathbf{N}(\mathbf{r})\,\mathrm{d}^3r,$$

and noting that $\mathbf{M} = \mathbf{m}/V$, we obtain

$$\iiint_{\mathbb{R}^3} \mathbf{N}(\mathbf{r})\cdot\mathbf{M}\,\mathrm{d}^3r = \iiint_{\mathbb{R}^3} \mathbf{N}(\mathbf{r})\,\mathrm{d}^3r\cdot\frac{\mathbf{m}}{V} \tag{28}$$

$$= \bar{\mathbf{N}}\cdot\mathbf{m}. \tag{29}$$

Therefore,

$$\boxed{\mathbf{m}^{\mathrm{B}} = \big(\mathbf{I}-\bar{\mathbf{N}}\big)\cdot\mathbf{m}}. \tag{30}$$

We now consider the two-dimensional analogue, where only the in-plane components of the fields are relevant. Starting from the constitutive relation $\mathbf{B} = \mu_0(\mathbf{H}+\mathbf{M})$, which holds component-wise also in 2D space, we define the in-plane "induction moment" as

$$\mathbf{m}_\perp^{\mathrm{B}} = \int_S \mathbf{B}_\perp\,\mathrm{d}a = \mu_0\int_S \big(\mathbf{H}_\perp+\mathbf{M}_\perp\big)\,\mathrm{d}a. \tag{31}$$

In the absence of external fields, $\mathbf{H}_\perp$ is purely the demagnetizing field, derivable from a scalar potential $\Phi$: $\mathbf{H}_\perp = -\boldsymbol{\nabla}\Phi$. In two dimensions the potential generated by a magnetization distribution is

$$\Phi(\mathbf{r}_\perp) = -\frac{1}{2\pi}\oint_C \frac{\hat{\mathbf{n}}' \boldsymbol{\cdot} \mathbf{M}_\perp(\mathbf{r}'_\perp)}{|\mathbf{r}_\perp - \mathbf{r}'_\perp|}\,\mathrm{d}\ell', \tag{32}$$

where $D$ is the boundary of the sample and $\hat{\mathbf{n}}'$ the unit tangent vector along $D$.

The demagnetizing field therefore becomes

$$\mathbf{H}_\perp(\mathbf{r}_\perp) = -\frac{1}{2\pi}\boldsymbol{\nabla}\oint_D \frac{\hat{\mathbf{n}}' \cdot \mathbf{M}_\perp(\mathbf{r}'_\perp)}{|\mathbf{r}_\perp - \mathbf{r}'_\perp|}\,\mathrm{d}\ell' \tag{33}$$

$$= -\Big(\frac{1}{2\pi}\boldsymbol{\nabla}\oint_D \frac{\hat{\mathbf{n}}'}{|\mathbf{r}_\perp - \mathbf{r}'_\perp|}\,\mathrm{d}\ell'\Big) \cdot \mathbf{M}_\perp(\mathbf{r}_\perp). \tag{34}$$

The quantity in parentheses defines the two-dimensional demagnetizing tensor

$$\mathbf{N}_\perp(\mathbf{r}_\perp) = \frac{1}{2\pi}\boldsymbol{\nabla}\oint_D \frac{\hat{\mathbf{n}}'}{|\mathbf{r}_\perp - \mathbf{r}'_\perp|}\,\mathrm{d}\ell'. \tag{35}$$

Hence $\mathbf{H}_\perp = -\mathbf{N}_\perp \boldsymbol{\cdot} \mathbf{M}_\perp$, and the in-plane induction is

$$\mathbf{B}_\perp = \mu_0\big(\mathbf{I} - \mathbf{N}_\perp\big) \boldsymbol{\cdot} \mathbf{M}_\perp. \tag{36}$$

Integrating over the sample area gives

$$\mathbf{m}_\perp^{\mathrm{B}} = \mu_0 \int_S \big(\mathbf{I} - \mathbf{N}_\perp(\mathbf{r}_\perp)\big) \cdot \mathbf{M}_\perp\,\mathrm{d}a \tag{37}$$

$$= \mu_0\Big[\mathbf{m}_\perp - \int_S \mathbf{N}_\perp(\mathbf{r}_\perp) \boldsymbol{\cdot} \mathbf{M}_\perp\,\mathrm{d}a\Big], \tag{38}$$

where $\mathbf{m}_\perp = \int_S \mathbf{M}_\perp\,\mathrm{d}a$ is the total in-plane magnetic moment.

For uniform in-plane magnetization, $\mathbf{M}_\perp = \mathbf{m}_\perp/S$, and we may introduce the surface-averaged demagnetizing tensor

$$\bar{\mathbf{N}}_\perp = \frac{1}{S}\int_S \mathbf{N}_\perp(\mathbf{r}_\perp)\,\mathrm{d}a.$$

Then

$$\int_S \mathbf{N}_\perp(\mathbf{r}_\perp)\cdot\mathbf{M}_\perp\,\mathrm{d}a = \bar{\mathbf{N}}_\perp \boldsymbol{\cdot} \mathbf{m}_\perp,$$

and consequently

$$\boxed{\mathbf{m}_\perp^{\mathrm{B}} = \mu_0\big(\mathbf{I} - \bar{\mathbf{N}}_\perp\big)\boldsymbol{\cdot}\mathbf{m}_\perp}\,. \tag{39}$$

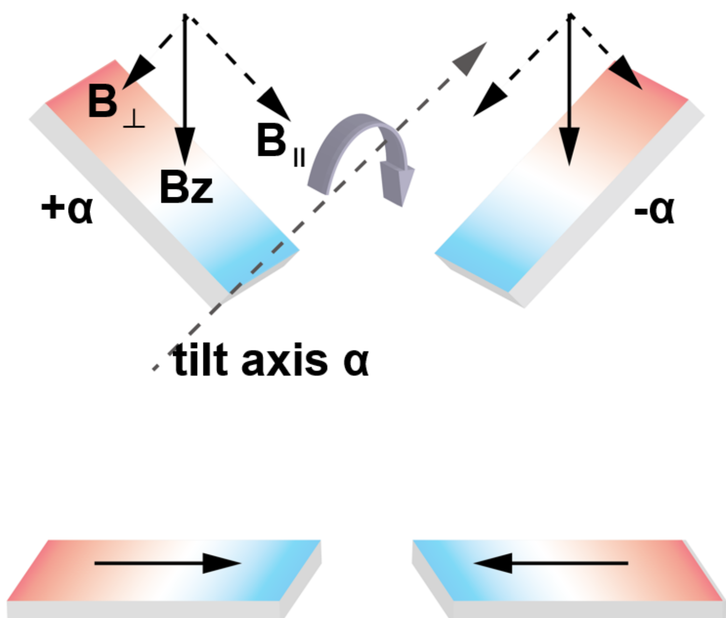


Figure S2: A schematic diagram illustrating the experimental setup for in situ magnetizing of a specimen within a transmission electron microscope (TEM).

**Alt text:** A schematic diagram of an in situ magnetizing procedure in a transmission electron microscope, showing specimen tilting under the objective-lens magnetic field and subsequent hologram acquisition after returning the specimen to zero tilt.

The magnetic phase shift, which constitutes the primary quantity of interest, must be isolated from the overlapping electrostatic contribution within the total measured phase. This separation was performed via an *in situ* magnetizing procedure employing sample tilting and the magnetic field of the objective lens, as illustrated in Figure S2.

The procedure involves acquiring electron holograms with the specimen magnetized in two precisely opposite directions. Magnetization reversal is achieved by first tilting the specimen to +70° and exciting the objective lens to apply a saturating field (up to 1.5 T). The lens is then deactivated, and the specimen is returned to its untilted (0°) orientation prior to hologram acquisition. An identical sequence is subsequently performed with a specimen tilt of $-70°$. This protocol ensures that the sample magnetization is fully saturated in opposite directions before the external field is removed, ideally resulting in two remnant magnetic states of equal magnitude but opposite orientation [4].

Under this condition, the electrostatic ($\phi_{\mathrm{E}}$) and magnetic ($\phi_{\mathrm{M}}$) phase contributions can be separated mathematically. Denoting the total phase images acquired in the two reversed states as $\phi_+$ and $\phi_-$, the components are given by:

$$\phi_{\mathrm{E}} = \frac{\phi_+ + \phi_-}{2}, \qquad \phi_{\mathrm{M}} = \frac{\phi_+ - \phi_-}{2}.$$

Thus, the electrostatic contribution is obtained from the half-sum, while the magnetic contribution is derived from the half-difference of the two phase images.

The magnetic moment of a linear four-particle $Fe_3O_4$ chain was subsequently measured. The magnetic phase, obtained using the same experimental and reconstruction procedure, is presented in Figure S3(a), with the corresponding projected in-plane magnetic induction shown as a phase contour map in Figure S3(b). The magnetic moment was quantified using circular, elliptical, and rectangular integration loops.

To improve accuracy, the measured moment was plotted against the squared loop radius and extrapolated to the zero-radius limit, as shown in Figure S3(c). Using the appropriate demagnetization factor for each loop geometry, the corrected magnetic moment values were calculated. Although the initially measured inductive moments, $\mathbf{m}^{\mathrm{B}}$, differ for each loop shape, the converted actual moment, $m$, values show strong agreement. This demonstrates that circular, elliptical, and rectangular integration loops can all yield reliable magnetic moment measurements, provided the corresponding demagnetization factors are correctly applied.

*Supplementary Note 4: Fresnel, noise and charging*

To assess the influence of Fresnel diffraction from the electrostatic biprism on the measurement accuracy, we systematically examined its effect on the loop integral of the magnetic moment using simulated electron holograms [5]. Figure S4(a) presents magnetic phase maps alongside their corresponding visualizations of the projected in-plane magnetic induction. The first panel shows the reference pure magnetic phase, corresponding to a magnetization of 1 T oriented at $\theta = 61.5°$ and free of other experimental artifacts, was first generated while panels 2–6 display the reconstructed magnetic phase maps were simulated using the same magnetic parameters but with varying biprism voltages. The corresponding reconstructed magnetic phases, obtained at biprism voltages of 250 V, 200 V, 150 V, 100 V, and 50 V, respectively. Analysis of these phase images reveals that as the biprism voltage decreases, phase errors induced by Fresnel diffraction become progressively more pronounced, affecting measurements across different radii.

Figure S4(b) summarizes the quantitative measurement results, with the value from panel 1 serving as the reference. The measured magnetic moment and its angular error are indicated in the figure. A significant increase in the error of the magnetic moment is observed as the biprism voltage decreases below 100 V, reaching 3.88% at 50 V. In contrast, the angular measurement remains largely unaffected, indicating that Fresnel diffraction primarily influences the magnitude rather than the direction of the measured magnetic induction.

Fresnel diffraction introduces a characteristic sine-like modulation in the hologram fringes, which manifests as periodic phase fluctuations upon reconstruction. These fluctuations propagate as systematic errors during the quantification process. Lower biprism voltages reduce the effective fringe width, thereby amplifying the relative contribution of Fresnel diffraction. This causes the interference fringes to broaden and blur, intensifying the phase modulation and consequently increasing the error in the measured magnetic moment.

These findings underscore the necessity of accounting for Fresnel diffraction in electron holography, particularly in low-voltage experiments. While our simulations show that post-processing corrections can partially mitigate these effects, they cannot eliminate them entirely. To ensure measurement accuracy, experimental parameters should be optimized—for instance, by using higher biprism voltages where feasible—and more advanced reconstruction algorithms that explicitly model diffraction effects should be employed to further reduce the associated errors.

To further investigate the influence of the signal-to-noise ratio (SNR) on measurement accuracy, we simulated a noise-free magnetic phase map as a reference (Figure S5(a) case 1) [5, 6]. Subsequently, a series of electron holograms were simulated with Fresnel diffraction effects included (at a fixed biprism voltage of 200 V) but with varying levels of additive noise. The corresponding reconstructed magnetic phase maps for SNRs of 29.34 dB, 25.25 dB, 22.74 dB, 16.16 dB and 13.22 dB are shown in Figure S5(a) case 2-6, respectively. The peak SNR is adopted, PSNR (dB) $= 10 \cdot \log_{10}\left(\frac{\mathrm{MAX}_I^2}{\mathrm{MSE}}\right)$, where $\mathrm{MAX}_I$ is maximum possible pixel value, MSE is mean squared error between original and noisy images, $\mathrm{MSE} = \frac{1}{MN}\sum_{i=1}^{M}\sum_{j=1}^{N}[I(i,j) - K(i,j)]^2$.

Analysis of these results reveals that as the SNR decreases, the fluctuation in the measured phase, and consequently the extracted magnetic moment, increases. This effect is particularly pronounced at lower SNR levels, where significant phase noise is evident. The fluctuations are more substantial at larger radii, indicating a spatially dependent impact of noise. Despite these fluctuations, the quadratic fitting method employed to extract the magnetic moment demonstrates considerable robustness, yielding measurements that remain relatively accurate even under low-SNR conditions. This suggests that while noise introduces variance, the underlying fitting procedure can effectively mitigate its systematic bias on the final result.

Quantitatively, Figure S5(b) shows that the error in the measured magnetic moment grows progressively as the SNR declines. At an SNR of 13.22 dB, for example, the magnetic moment error reaches 1.58%, while the associated azimuth angle error remains small at 0.85°. Although the phase profiles exhibit increased random fluctuations with added noise—particularly noticeable at larger radii—the subsequent quadratic fitting procedure stabilizes the extracted magnetic moment. This demonstrates the inherent robustness of the loop-integral method, which effectively averages over local noise variations to yield reliable results.

In summary, while Gaussian noise elevates measurement uncertainty, the magnetic-phase loop-integral method maintains considerable accuracy due to its noise-tolerant fitting approach. The method's ability to deliver stable measurements under significant noise interference underscores its practical utility in experimental electron holography.

We simulated the effect of electrostatic charging on magnetic phase images and analyzed its impact on magnetic moment quantification at different charge levels. Figure S6(a) illustrates simulated magnetic phase maps with increasing superimposed charging, alongside the corresponding measured magnetic moments. In the absence of charging, the measured magnetic moment is largely independent of the precise position of the integration loop within the sample. However, as demonstrated in Figure S6(b), the introduction of a charging phase gradient introduces a pronounced positional dependence, that is, the measured error increases with both the magnitude of the charge and the distance of the integration loop from the charge center. The sensitivity of this method is sufficient to detect the influence of even a single localized charge.

## References


[1] M. Beleggia, T. Kasama, R. E. Dunin-Borkowski, The quantitative measurement of magnetic moments from phase images of nanoparticles and nanostructures—I. fundamentals, Ultramicroscopy 110 (5) (2010) 425–432. doi:10.1016/j.ultramic.2009.10.007.

[2] M. Beleggia, M. De Graef, Y. T. Millev, D. A. Goode, G. Rowlands, Demagnetization factors for elliptic cylinders, Journal of Physics D: Applied Physics 38 (18) (2005) 3333. doi:10.1088/0022-3727/38/18/001.

[3] J. D. Jackson, Classical Electrodynamics, 3rd Edition, John Wiley & Sons, 1998.

[4] R. E. Dunin-Borkowski, M. R. McCartney, D. J. Smith, S. Parkin, Towards quantitative electron holography of magnetic thin films using in situ magnetization reversal, Ultramicroscopy 74 (1-2) (1998) 61–73. doi:10.1016/S0304-3991(98)00023-0.

[5] K. Yamamoto, T. Tanji, M. Hibino, Hologram simulation for off-axis electron holography, Ultramicroscopy 85 (1) (2000) 35–49. doi:10.1016/S0304-3991(00)00042-5.

[6] F. Roder, A. Lubk, D. Wolf, T. Niermann, Noise estimation for off-axis electron holography, Ultramicroscopy 144 (2014) 32–42. doi:10.1016/j.ultramic.2014.04.002.

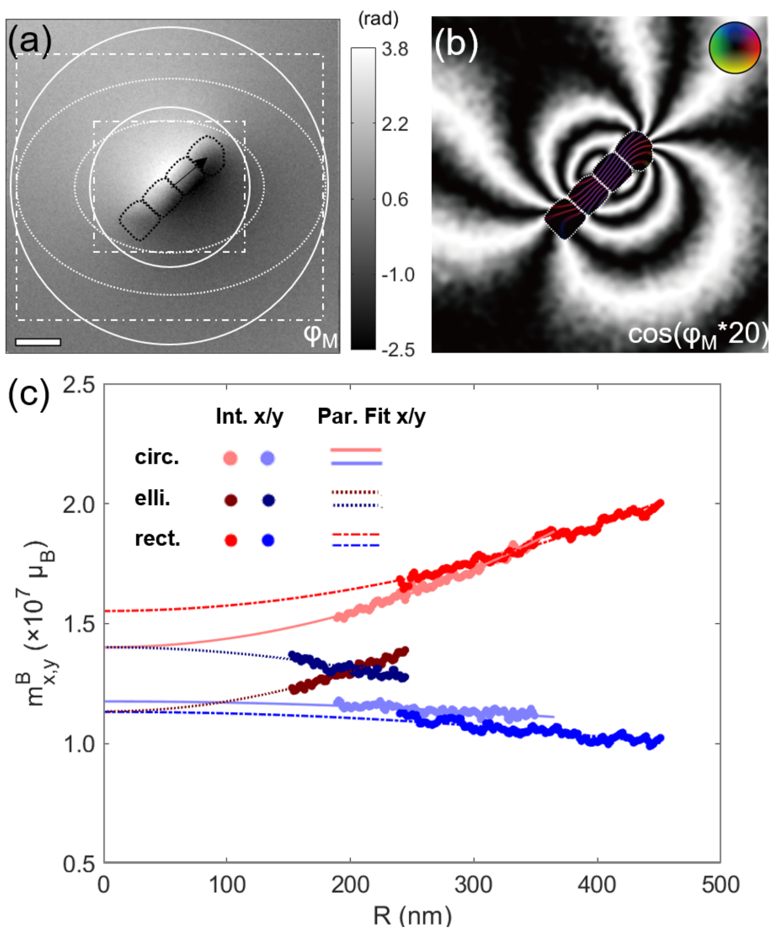


Figure S3: **Quantitative analysis of magnetic moments in four $Fe_3O_4$ nanoparticles via phase integration.** (**a**) Experimental magnetic phase shift map ($\varphi_m$) acquired from four $Fe_3O_4$ nanoparticles. Representative integration paths (circular (solid), elliptical (dashed), and rectangular (dotted)) are overlaid at the minimum and maximum radii used for analysis. Scale bar is 100 nm. (**b**) Visualization of the projected in-plane magnetic induction, represented by the contour map $\cos(20 \times \varphi_m)$. The color scheme indicates the direction of the magnetic field, highlighting the dipole-like structure of each nanoparticle's stray field. (**c**) Quantified in-plane inductive moment components ($m^{\mathrm{B}}_{x,y}$) for each nanoparticle, extracted from the closed-path phase integrations in (**a**) using circular, elliptical, and rectangular paths. The comparison demonstrates the robustness of the measurement to the choice of integration geometry.

**Alt text:** A multi-panel figure showing quantitative magnetic moment analysis of four $Fe_3O_4$ nanoparticles. The panels include an experimental magnetic phase map with different closed integration paths, a phase-contour visualization of the projected in-plane magnetic induction, and plots of extracted magnetic moment components for different path geometries.

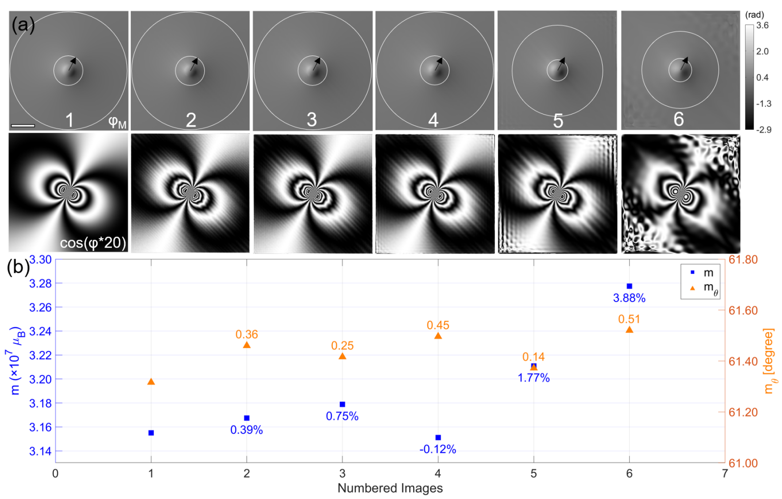


Figure S4: **Effect of Fresnel diffraction on quantitative magnetic moment retrieval from electron holography. (a)** Reconstructed magnetic phase (top) and corresponding projected magnetic induction maps (bottom) for simulations with varying biprism voltages (50–250 V). Case 1 is the reference without Fresnel diffraction; cases 2–6 include its effects at specified voltages. **(b)** Comparison of magnetic moments extracted from the phase reconstructions in (a), obtained by evaluating circular loop integrals of the reconstructed phase and determining the magnetic moment via quadratic (parabolic) fitting and extrapolation; the deviation from the reference value increases as Fresnel diffraction becomes more pronounced.

**Alt text:** A multi-panel simulation figure comparing reconstructed magnetic phase and projected magnetic induction maps under different biprism voltages. The accompanying plots show how the extracted magnetic moment changes as Fresnel diffraction effects become stronger.

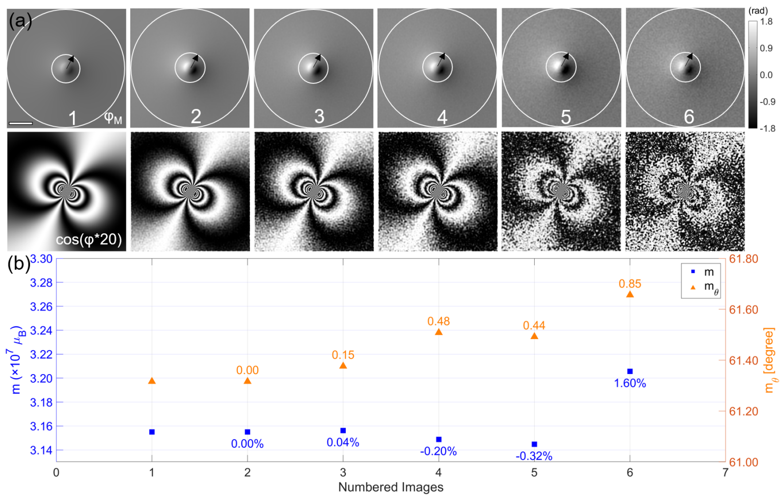


Figure S5: **Effect of phase noise on magnetic moment quantification. (a)** Reference simulated magnetic phase image without noise (case 1) and Magnetic phase images with progressively increasing noise, corresponding to signal-to-noise ratios (SNRs) of 29.34, 25.25, 22.74, 16.16, and 13.22 dB (case 2-6), overlaid with phase contours ($\cos(\phi \times 20)$). **(b)** Results of the closed-path integration performed on each image in (a), showing increased measurement variance with noise.

**Alt text:** A multi-panel simulation figure showing magnetic phase images with increasing phase noise and corresponding phase-contour overlays. The accompanying plots compare closed-path integration results at different signal-to-noise ratios.

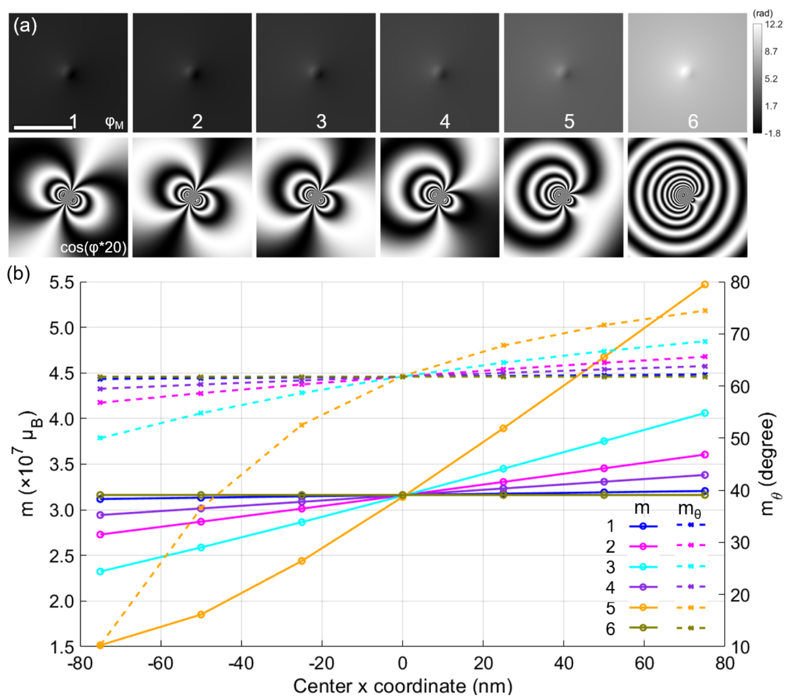


Figure S6: **Systematic quantification of charging artifacts in phase-based magnetometry.** **(a)** Reference simulated magnetic phase and phase-contour maps (case 1) compared to those perturbed by increasing levels of sample charging (cases 2-6: 1 to 50 charges). **(b)** Resulting deviation in the measured magnetic moment, plotted against loop position for each charge condition, demonstrating the positional sensitivity of the charging artifact.

**Alt text:** A multi-panel simulation figure showing magnetic phase and phase-contour maps with increasing levels of localized electrostatic charging. The accompanying plots show the resulting changes in the measured magnetic moment as a function of integration-loop position.